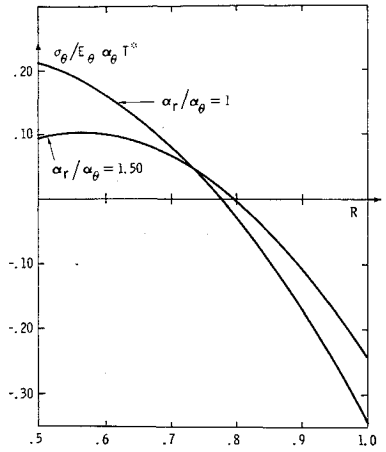

Fig. 1 Circumferential stress.

where

$$K_{1m} = \frac{c_{44}[m\lambda_2 c_{11} - (m\lambda_1 - \lambda_2)c_{12} - \lambda_1 c_{22}]}{c_{11}c_{44}(m+1)^2 + c_{12}^2 + 2c_{12}c_{44} - c_{11}c_{22} - c_{11}c_{44} - c_{22}c_{44}} \quad (9c)$$

$$k_{1j} = \frac{(c_{11}c_{22} - c_{12}^2 - c_{12}c_{44})P_{1j} + (c_{12} - c_{22})c_{44}}{-c_{11}c_{44}P_{1j} + c_{11}c_{22} - c_{12}^2 + (c_{11} - c_{12})c_{44}} \quad j = 1,2 \quad (9d)$$

The denominator of K_{1m} has a zero when $m + 1 = P_{11}$ or $m + 1 = P_{12}$. When this condition occurs, either a different particular solution term must be found or a suitable limiting process invoked. This situation implies a specific relation among the elastic constants, and since these are experimentally determined as discussed previously for the case $n = 0$, it will be assumed that this required relationship is not met. Also, h_{11} and k_{11} can be indeterminant, but again, this requires that the elastic constants satisfy a special relation.

Solution for n ≥ 2

For $n \geq 2$ the R dependent terms of Eqs. (4a) take the form

$$U_n(R) = \sum_{j=1}^{4} A_{nj}R^{P_{nj}} + \sum_{m=0}^{\infty} D_{nm}T_{nm}R^{m+1}$$
$$V_n(R) = \sum_{j=1}^{4} h_{nj}A_{nj}R^{P_{nj}} + n\sum_{m=0}^{\infty} E_{nm}T_{nm}R^{m+1} \quad (10)$$

and the associated $S_r^n(R)$, $S_\theta^n(R)$, and $S_{r\theta}^n(R)$ may be obtained from Eqs. (1). In Eq. (10), the P_{nj} are the four roots of

$$P_{nj}^4 + \frac{[n^2(c_{12}^2 + 2c_{12}c_{44} - c_{11}c_{22}) - (c_{11} + c_{22})c_{44}]}{c_{11}c_{44}}P_{nj}^2 + (n^2 - 1)^2\frac{c_{22}}{c_{11}} = 0 \quad (11)$$

and the A_{nj} are arbitrary constants. The traction free boundary conditions at $R = a/b$ and $R = 1$ render four simultaneous equations for the determination of the A_{n1}, A_{n2}, A_{n3} and A_{n4}. The solution of these equations is quite lengthy and will not be presented. It should be noted here that the P_{nj} may be real or complex. If they are complex, they occur as complex conjugate pairs and the associated A_{nj} must also be complex conjugate pairs to insure that the displacements and stresses be real.

Summary and Numerical Results

Formulas for the thermal stresses in a transversely isotropic, hollow circular cylinder have been derived for the temperature distribution $T(R, \theta)$ given by Eq. (3). Explicit formulas are presented for $n = 0$ in Eqs. (7) and for $n = 1$ in Eqs. (9); results for higher harmonics can be obtained from Eqs. (10).

Circumferential stress components for a cylinder with a/b = 1/2, $E_r/E_\theta = 0.970$, $G_{r\theta}/E_\theta = 0.500$, $\nu_{z\theta} = \nu_{\theta r} = 0.10$ are presented in Fig. 1 for $\alpha_r/\alpha_\theta = 1.00$, 1.50, and the temperature distribution $T = T^*(1 - 2R + 2R^2)$. These material properties are typical for ATJ graphite. As previously mentioned, the Young's moduli and Poisson's ratios are related to c_{ij}; e.g., see Ref. 4.

References

[1] Forray, M., "Thermal Stresses in Rings," *Journal of the Aerospace Sciences*, Vol. 26, No. 5, May 1959, pp. 310–311.

[2] Forray, M., "Formulas for the Determination of Thermal Stresses in Rings," *Journal of the Aerospace Sciences*, Vol. 27, No. 3, March 1960, pp. 238–240.

[3] Forray, M., "Table for Thermal Stresses in Rings," *Journal of the Aerospace Sciences*, Vol. 27, No. 6, June 1960, pp. 478–479.

[4] Terner, E., "On Thermal Stresses in Certain Transversely Isotropic, Pyrolytic Materials," *Proceedings of the Fourth U. S. National Congress of Applied Mechanics*, American Society of Mechanical Engineers, New York, 1962, Vol. 2, pp. 1147–1152.

[5] Eubanks, R. A. and Sternberg, E., "On the Axisymmetric Problem of Elasticity Theory for a Medium with Transverse Isotropy," *Journal of Rational Mechanics and Analysis*, Vol. 3, 1954, pp. 89–101.

Laminar Reynolds Analogy Factor on a Sharp Flat Plate at Mach 10.4

HOWARD W. STONE*
NASA Langley Research Center, Hampton, Va.

THERE are several theoretical variations of Reynolds analogy factor ($2N_{St}/C_f$), but a simple and often used value at hypersonic speeds is the Colburn value of the Prandtl number to the $-\frac{2}{3}$ power. Only a few published studies, however, attempt to determine the validity of this value under various flow conditions. It is the purpose of this Note to present some values measured on a sharp flat plate in a Mach 10.4 boundary-layer induced-pressure gradient and to show, by theoretical calculations, the effect of the wall-pressure and wall-temperature gradients that are present in the experiment.

Two 30-in.-long sharp-edge flat plates of aspect ratio 0.5 with identical exterior dimensions were tested in the continuous flow hypersonic tunnel at the NASA Langley Research Center. The thinner plate (0.031 in. thick) was instrumented with thermocouples to obtain heat transfer by the transient calorimeter technique. The thicker plate (0.187 in. thick) was instrumented to obtain the wall-pressure distribution and was used with traversing probes to obtain boundary-layer impact pressure profiles. The heat-transfer test interval was about five seconds whereas the wall-pressure measurements and boundary-layer profiles required about two minutes of exposure to the hypersonic stream. A more complete description of the models and tests and the resultant velocity profiles and heat-transfer distributions are presented in Ref. 1.

The theoretical approach used to calculate wall-pressure gradient and wall-temperature gradient effects was an implicit finite difference solution to the compressible laminar boundary-layer equations for a perfect gas and a Sutherland

Received June 6, 1969.

* Aerospace engineer, Hypersonic Aerodynamics Branch, Aerophysics Division.

viscosity-temperature relationship.[2] In applying this solution, the measured total pressure at the boundary-layer edge was used. The calculated skin-friction coefficient and Stanton number distributions for a uniform wall temperature and pressure are shown as solid lines in Fig. 1. Although most of the model surface temperatures remained relatively unchanged, the thin 20° bevel leading edge surely was hotter. The calculated Stanton number and skin-friction coefficient resulting from the estimated wall-temperature distribution (Fig. 1a) are shown by the dashed curves. The skin friction was essentially unchanged by the hot leading edge, but the Stanton number increased even far downstream of the leading edge.

The measured wall-pressure distribution was extrapolated to the leading edge using first-order boundary-layer interaction theory (see insert Fig. 1b). A pressure plateau was assumed to be reached at the leading edge when $M_\infty/(R_{\infty x})^{1/2}$ reached a value of 0.25. This wall-pressure distribution, when used in the finite difference solution, resulted in skin friction and Stanton numbers lower than the uniform wall-pressure conditions (Fig. 1b). The combined effect of the wall-pressure and wall-temperature gradients is shown in Fig. 1c. The skin-friction coefficient is increased near the leading edge, but crosses the curve for the uniform wall conditions while the Stanton number is increased over the whole model length.

Calculated Reynolds analogy factors are shown as shaded regions in Fig. 2. The lower edge of the shaded region represents the values for the measured wall-pressure and uniform wall-temperature conditions. The upper edge represents the values for combined conditions of the hot leading edge and the measured wall-pressure distribution.

The experimental Reynolds analogy values in Fig. 2 are formed from the measured heating and the skin friction determined from the boundary-layer profile. A typical measured boundary-layer velocity profile and a theoretical profile are shown in Fig. 3. The high velocity points near the wall result from wall-probe interaction and possibly a very low Reynolds number effect. The first "good" point was used to obtain the maximum experimental range of the

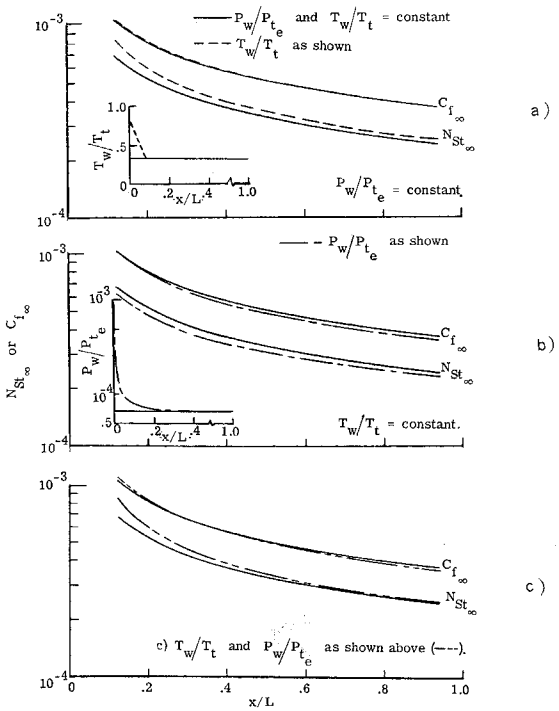

Fig. 1 The effect of wall-pressure gradient and wall-temperature gradient on the skin-friction coefficient and Stanton number based on freestream conditions: $R_{\infty,L} = 3.68 \times 10^6$.

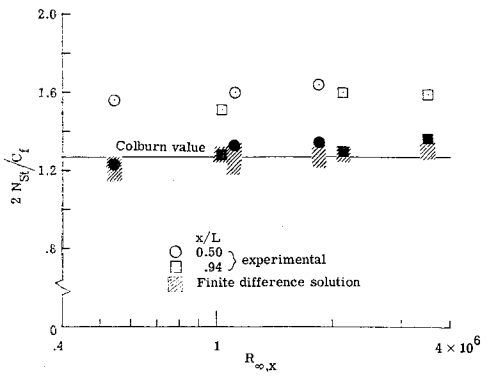

Fig. 2 Reynolds analogy factor based on local conditions. Open symbols obtained using straight line; solid symbols obtained considering nonlinearity.

velocity gradient at the wall. The minimum value was determined from a straight line drawn between the first "good" point and the origin. To estimate the effect of the nonlinear velocity, the change in gradient of the theoretical velocity distribution between the "good" point and wall was added to the straight-line value. All reasonable fairings resulted in values of the wall shearing stress between these two values. The data of Fig. 2 represented by the open symbols were obtained using the slope of the straight line in the wall shearing stress. The darkened symbols represent the data obtained by including the difference of the slopes in the theoretical profile.

The straight-line value of the velocity gradient at the wall provided a satisfactory value of skin friction in some previous lower Mach number investigations. However, this technique resulted in Reynolds analogy factors approximately 25% higher than the Colburn value in this experiment. Theory predicts a nonlinear velocity distribution in a Mach 10.4 boundary layer induced pressure gradient that appears consistant with the data, and the experimental Reynolds analogy factors obtained using the theory to account for the nonlinearity near the wall are in agreement with those derived from the finite difference solution. Although this procedure does not provide true experimental verification, agreement between theory and experiment is of little doubt. Furthermore, the Colburn Reynolds analogy factor appears to be a valid estimate for these flow conditions.

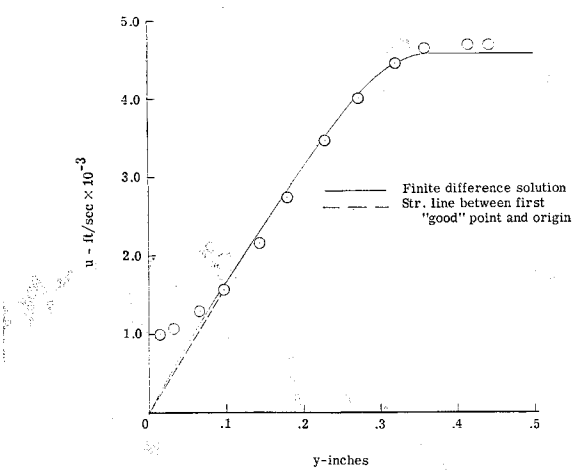

Fig. 3 Typical boundary-layer velocity distribution: $R_{\infty,x} = 1.12 \times 10^6$.

References

[1] Stone, H. W., "The Leading-Edge Effects on the Laminar Flat-Plate Boundary Layer and the Aerodynamic Heating at Mach 10.4," TN D-5160, May 1969, NASA.

[2] Hamilton, H. H., II, "A Theoretical Investigation of the Effect of Heat Transfer on Laminar Separation," Master's thesis, May 1969, Dept. of Aerospace Engineering, Virginia Polytechnic Institute.

Particle Removal in the Ablation of Artificial Graphite

HOWARD G. MAAHS* AND DAVID R. SCHRYER*
NASA Langley Research Center, Hampton, Va.

Introduction

IN considering the ablation behavior of polycrystalline, artificial graphite in dynamic, oxidizing environments, it is becoming increasingly evident that conventional thermochemical phenomena are frequently inadequate to explain the total observed erosion.[1–6] Various investigators have theorized that mechanical and aerodynamic removal of particulate matter occurs in addition to oxidation and may be caused by vibration,[2] aerodynamic shear,[3–5] and pressure gradients.[5]

Evidence offered in support of this mechanical and aerodynamic removal has been circumstantial in nature, i.e., after-test surfaces that are rough and irregular, greater observed erosion than can be accounted for by thermochemical calculations, and greater erosive effect of higher pressure environments. Recently, however, direct experimental evidence has been obtained at this laboratory. The purpose of this Note is to present this direct evidence of particle removal as well as evidence that such removal is linked to oxidation. Also presented is a theoretical mechanism relating particle removal to oxidation.

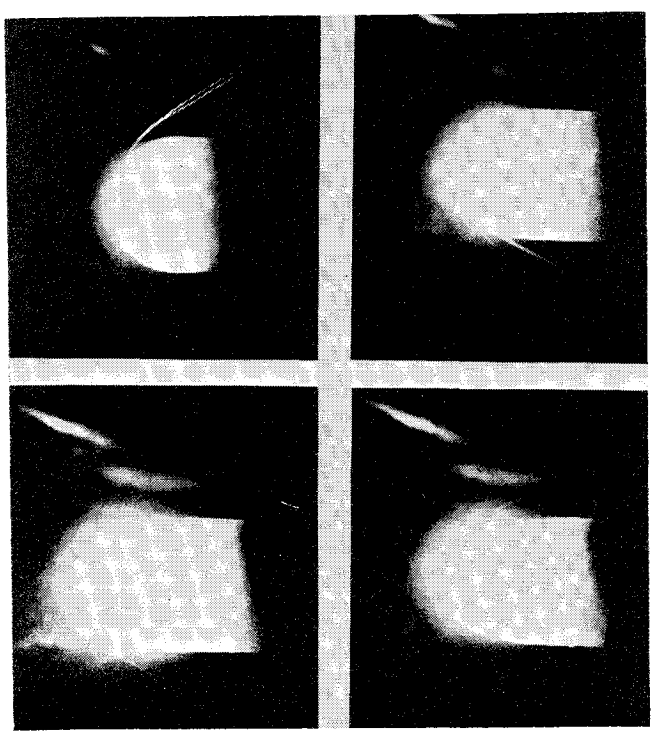

Fig. 1 Luminous traces from an eroding graphite specimen.

Received June 12, 1969.
* Aerospace Technologist.

Data and Observations

Figure 1 presents a chronological sequence of four frames from close-up, high-speed motion pictures (220 pictures/sec) of a graphite specimen eroding in a high-temperature Mach 2.5 airstream (stagnation-point cold wall heating rate 565 w/cm^2, stagnation pressure 5.6 atm). Figure 1 clearly shows luminous traces of particles leaving the surface. As time progresses, the surface acquires an irregular configuration. By means of much higher-speed motion pictures (average 5500 pictures/sec) as many as 250 separate traces have been observed leaving an eroding surface during 1 sec of ablation. This number is conservative because many escaping particles are too small to observe or are obscured by the specimen or its luminosity; however, the order of magnitude illustrates the extent to which particle removal can contribute to total erosion.

It is recognized, of course, that such luminous traces from an ablating surface have been observed previously in the case of charring ablators. This series of photographs is, however, the first known direct photographic evidence for graphite—a material which has considerably greater mechanical integrity than hydrocarbon chars and, in addition, lacks the internal generation of pyrolysis gases, which is sometimes held responsible for the removal of pieces of char. Estimates of particle sizes from these observations indicate the largest particles to be on the order of one-half the maximum size of a filler grain. It is suspected that the majority of particles lost consist of grains or partially oxidized grains with only rare instances of agglomerates of grains being lost.

Direct photographic observation of particle removal is more frequent at higher stagnation pressures than at lower pressures. However, even at lower pressures, in cases in which direct photographic observation of particles has not been achieved, circumstantial evidence for particle removal is often strong (i.e., after-test surfaces are rough and pitted). In these cases, it is believed that the particles removed consist largely of partially oxidized filler grains too small to be seen by the photographic techniques employed.

The mechanical and aerodynamic forces that cause particle removal are not, by themselves, solely responsible for such removal. They must be accompanied by oxidation. This is demonstrated by tests made in both oxidizing and inert heated test streams. Figure 2 presents a photograph of an untested graphite specimen in comparison with specimens tested in nitrogen and air. The greatly increased erosion of the specimen tested in air is evident. The rough, irregular surface of this specimen is characteristic of a significant degree of particle removal. The specimen tested in nitrogen has undergone negligible erosion, but the difference in its surface appearance from the untested specimen indicates that some material, perhaps already loose, has been removed from the surface. High-speed motion pictures taken during the tests of these specimens indicate appreciable particle removal only from the specimen in the oxidizing environment. Furthermore, photomicrographs of sections through the surfaces of these specimens (Fig. 3) show considerable roughness and protruding grains associated with the specimen tested in air, whereas the surface of the specimen tested in nitrogen is similar to that of the untested specimen. These results lead to the conclusion that it is necessary for oxidative weakening of

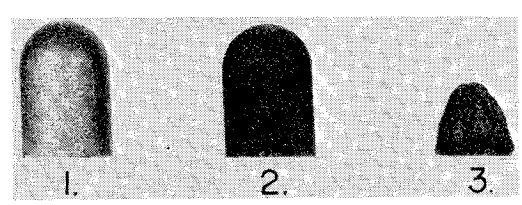

Fig. 2 Comparison of graphite specimens: 1) untested, 2) tested in nitrogen, 3) tested in air.